communications physics

A Nature Portfolio journal

Article

https://doi.org/10.1038/s42005-025-02390-w

# Characterisation of turbulence suppression by fast-ion-Alfvénic instability

Check for updates

Akihiro Ishizawa [1] ✉, Emanuele Poli[2], Alessandro Di Siena[2] & Taik Soo Hahm[3]

Turbulence causes anomalous transport of plasma and thus limits achieving high temperature and density of magnetically confined fusion plasmas. Recently, fast-ion-driven Alfvénic instabilities were found to influence plasma thermal confinement by regulating turbulence. However, both favourable and unfavourable effects coming from various mechanisms have been reported from experiments and simulations to date. Here, we report a key parameter (ratio between growth rate of Alfvénic instability and that of microturbulence) which can characterise changes in heat transport of thermal ions due to nonlinear interaction between the fast-ion-driven Alfvénic instabilities and microturbulence in tokamak plasmas. The transition from transport enhancement to reduction occurs at a particular value of the parameter as it gets higher, and is reminiscent of the bifurcation responsible for transport-barrier formation. This simple characterisation successfully covers the trend of experimental results, and can provide a useful guideline for realising high performance confinement of burning plasmas in which fast ions are abundant.

For thermonuclear fusion of magnetically confined plasmas, one needs to achieve high plasma temperature, density, and energy confinement time simultaneously. One primary reason limiting this goal has been anomalous plasma transport, which is caused by low-frequency, short-scale microturbulence[1].

Fast ions produced by external heating methods such as neutral beam injection (NBI) and ion cyclotron resonance heating (ICRH) sometimes excite high-frequency Alfvénic eigenmodes (AEs)[2], which are magnetohydrodynamic (MHD) modes at the macroscale (device size). They can degrade confinement of fast ions[3–7], and therefore have been traditionally thought to be a threat to achieving fusion[8–10]. While they have been sometimes observed to degrade confinement of thermal plasma as well[11–13], there is accumulating evidence that the fast ion-driven AEs can sometimes enhance confinement of thermal plasmas[14–22]. Recently, there has been a lot of progress in research addressing this subject[17,23,24]. However, there have been no publication that clarifies these two opposing trends to date, and it is important to understand the underlying physics responsible for those. A simple characterisation of the condition under which we expect the thermal confinement enhancement in the presence of the fast ion-driven AEs will be useful for extrapolation to future devices in which fast ions will be abundant.

This study concentrates on cases in which AEs and microturbulence coexist, and their nonlinear interaction is considerable. We note that theoretically, fast ions can enhance thermal plasma confinement in the absence of AEs as well[25–30]. We emphasise that AE–microturbulence interaction is not only fusion-relevant, but also of high academic interest by itself as a prime example of multi-scale interaction in plasmas[11–16,18,19,22,31,32]. Indeed, similar problems have been a subject of active research in space and astrophysics[33–35].

In this paper, we present state-of-the-art global gyrokinetic simulation results on nonlinear interactions between toroidal Alfvénic eigenmode (TAE) and turbulence driven by ion-temperature gradient (ITG) in tokamak plasmas. TAE and ITG are the leading candidates for AEs and microturbulence, respectively, in present-day experiments. Here, TAE is the standing Alfvén wave formed by the toroidal coupling, which renders the continuum damping ineffective, and can be excited by the resonance with the fast ions[3]. We have found a dimensionless parameter that successfully characterises the changes in turbulent heat transport due to the TAE–turbulence interactions. The parameter is the ratio of the linear growth rate of TAE to that of turbulence, $\gamma_{\mathrm{TAE}}/\gamma_{\mathrm{Turb}}$. The transport increases at low values of $\gamma_{\mathrm{TAE}}/\gamma_{\mathrm{Turb}}$, whereas it is reduced at high values of $\gamma_{\mathrm{TAE}}/\gamma_{\mathrm{Turb}}$. The transition from the enhancement to the reduction occurs at $\gamma_{\mathrm{TAE}}/\gamma_{\mathrm{Turb}} \simeq 0.5$, and can provide an understanding of the opposite predictions on the heat transport of thermal ions described above. This parameter characterisation is in good agreement with the trend of experimental results indicating the influence of a variety of AEs on the thermal heat transport in the Joint European Torus (JET),

[1]Graduate School of Energy Science, Kyoto University, Kyoto, Japan. [2]Max Planck Institute for Plasma Physics, Garching, Germany. [3]Nuclear Research Institute for Future Technology and Policy, Seoul National University, Seoul, Republic of Korea. ✉e-mail: ishizawa@energy.kyoto-u.ac.jp

the Axially Symmetric Divertor Experiment (ASDEX)-Upgrade, and the Doublet III-D (DIII-D).

The reduction in the transport at high values of $\gamma_{TAE}/\gamma_{Turb}$ is due to the shearing of microturbulence eddies by the large-scale E × B flow associated with TAE. This transition from TAE-induced thermal transport increase at low values of $\gamma_{TAE}/\gamma_{Turb}$ to TAE-induced thermal transport reduction at high values of $\gamma_{TAE}/\gamma_{Turb}$ is reminiscent of the well-known bifurcation in transport-barrier formation[36], in which $\omega_{E\times B}/\gamma_{Turb}$ plays the role of an order parameter[37,38]. Here, $\omega_{E\times B}$ is the E × B shearing rate, and $\gamma_{Turb}$ represents the ambient microturbulence decorrelation rate, which can be approximated by the growth rate of turbulence.

## Results

### Simulation of TAE–microturbulence interaction

The turbulent transport in the presence of interactions between microturbulence and the Alfvénic eigenmode is simulated using the GKNET code[39] based on nonlinear gyrokinetic theory[40,41]. See the "Methods" section for the numerical model and plasma parameters.

In the tokamaks, the plasma temperature is high in the core region (small $r$ in Fig. 1a) and low in the edge region (large $r$ in Fig. 1a). The ion-temperature gradient (ITG) drives microinstability with the linear growth rate $\gamma_{Turb}$, which then develops into microturbulence at the ion-Larmor radius scale, as shown by small-scale eddies (Fig. 1a) in a turbulent steady state established as a result of complex processes, including the production of large-scale flow, such as zonal flow[38]. The fluctuating E × B velocity due to the perturbed electrostatic potential $\phi$ in Fig. 1a causes the thermal ion heat flux in the radial direction. On the other hand, the fast ion density gradient produced by external heating drives the toroidal Alfvénic eigenmode (TAE) with the linear growth rate $\gamma_{TAE}$, which in turn produces large-scale eddies, as shown in Fig. 1c. Figure 1b shows that the presence of TAE significantly influences turbulence. The influence of the TAE on the zonal flow shearing rate is shown in Fig. 1d and is discussed later. To investigate the changes in the thermal heat flux due to the TAE–turbulence interaction, we compare the thermal ion heat transport due to turbulent fluctuations with a fast-ion-driven TAE in Fig. 1b and without the TAE in Fig. 1a.

To understand a general trend of changes in the heat transport, nonlinear gyrokinetic simulations were performed for several plasma profiles with different thermal ion-temperature and fast ion-density gradients represented by the logarithmic gradients $1/L_T = -\mathrm{d}\ln T/\mathrm{d}r$ and $1/L_{nf} = -\mathrm{d}\ln n_f/\mathrm{d}r$, respectively. For example, a steep thermal temperature gradient corresponds to a large $1/L_T$ value. In addition, microturbulence is simulated for different values of normalised plasma pressure $\beta = 2\mu_0 nT/B^2$ (ratio of thermal to magnetic pressure) to understand a common trend of changes in the heat transport due to the ITG turbulence at low $\beta$ ($\beta = 0.64\%$) and kinetic ballooning mode (KBM) turbulence at high $\beta$ ($\beta = 1.28\%$). The KBM is also a microinstability driven by an ion-temperature gradient, but has stronger magnetic fluctuations than the ITG turbulence. The effect of nonlinear TAE–turbulence interaction on the heat flux of thermal ions $Q_i$ is evaluated by comparing $Q_i$ in the presence of fast ions (Fig. 1b) indicated by "TAE + Turb" and $Q_i$ in the absence of fast ions (Fig. 1a) indicated by "Turb". See the "Methods" section for quantitative descriptions of $Q_i$, $\gamma_{TAE}$, and $\gamma_{Turb}$.

### Parameter characterising heat transport change

We summarise the impact of the interactions between the TAE and turbulence on the heat flux of thermal ions $Q_i$ in Fig. 2. A key dimensionless

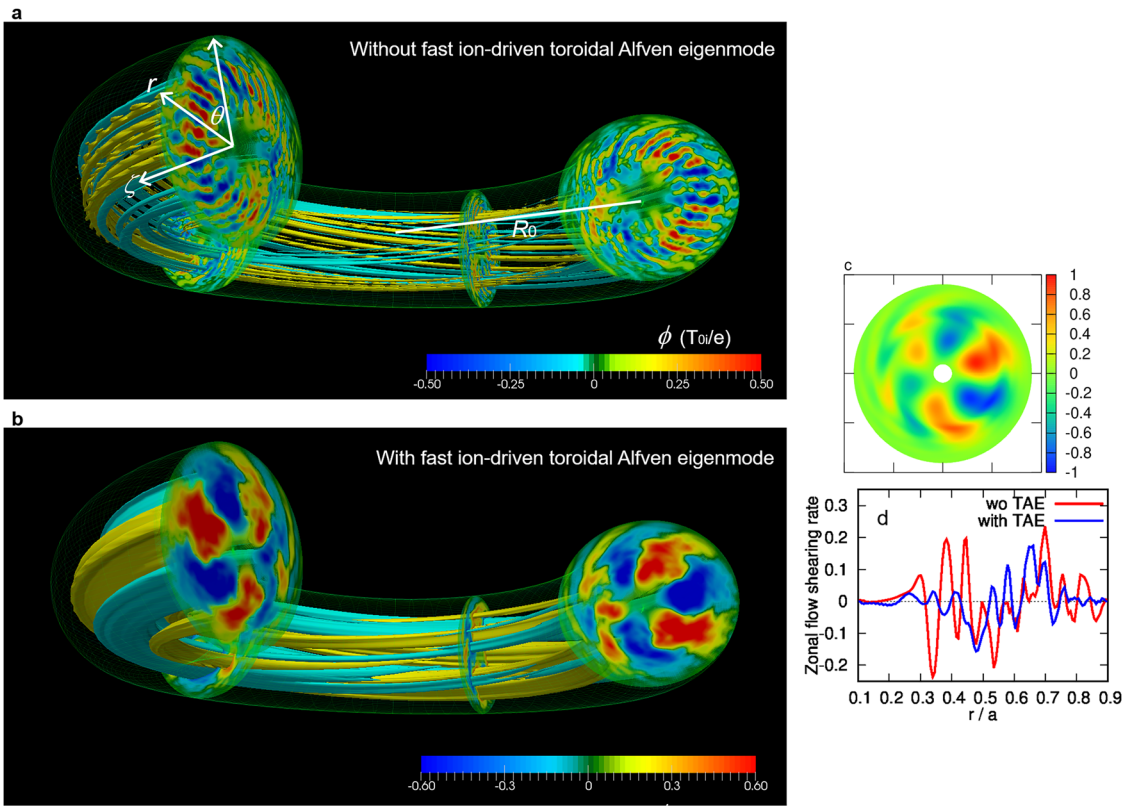



**Fig. 1 | Microturbulence with/without fast ion-driven Alfvén eigenmode in a tokamak plasma. a** Contour plots of perturbed electrostatic potential $\phi$ in microturbulence without toroidal Alfvénic eigenmode (TAE) simulated using the global nonlinear gyrokinetic simulation code GKNET. **b** Contour plots of perturbed electrostatic potential in microturbulence with TAE driven by fast ions. The presence of the TAE significantly influences microturbulence as a result of the nonlinear TAE–turbulence interaction. Here, $r$, $\theta$, and $\zeta$ are the minor radius, the poloidal and toroidal angles, respectively, and $R_0$ is the major radius of the torus. The ratio of fast ion to bulk ion temperature is $T_{0f}/T_{0i} = 25$, and the fraction of fast ion density normalised to electron density is $n_{0f}/n_{0e} = 2.5\%$. **c** Contour plots of perturbed electrostatic potential of the TAE eigenfunction. **d** Profiles of zonal flow shear with and without TAE.

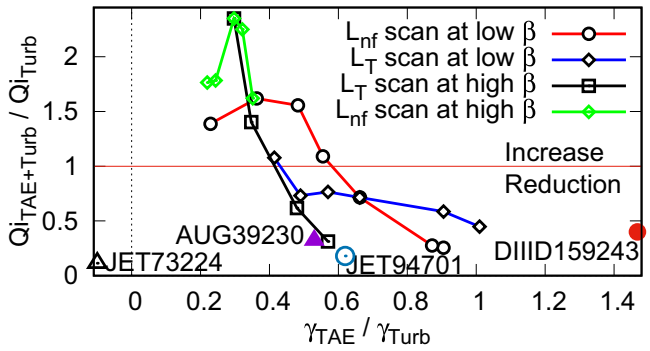



**Fig. 2 | Influence of fast-ion-driven Alfvénic eigenmodes on turbulent transport characterised by the key dimensionless parameter.** Thermal ion heat flux with fast ions $Q_{iTAE+Turb}$ normalised to that without fast ions $Q_{iTurb}$ as a function of $\gamma_{TAE}/\gamma_{Turb}$, where $\gamma_{TAE} = \gamma$ ($n = 2$) and $\gamma_{Turb} = \gamma$ ($n = 12$) are the linear growth rates of the TAE and the microturbulence, respectively, where $n$ is the toroidal wavenumber. Four curves with points correspond to the four scans of GKNET simulations for various plasma profiles: the fast-ion density gradient $L_{nf}$ scan of the turbulence at low normalised plasma pressure $\beta$, the thermal temperature gradient $L_T$ scan of the turbulence at low $\beta$ ($\beta = 0.64\%$), the $L_T$ scan of the turbulence at high $\beta$ ($\beta = 1.28\%$), and the $L_{nf}$ scan of the turbulence at high $\beta$. Symbols ▲ AUG39230, ⊙ JET94701, • DIII-D159243, and △ JET73224 are from the analysis of experimental data. The heat flux is increased due to the TAE–turbulence interaction $Q_{iTAE+Turb}/Q_{iTurb} > 1$ at low values of $\gamma_{TAE}/\gamma_{Turb}$. On the other hand, the heat flux is reduced $Q_{iTAE+Turb}/Q_{iTurb} < 1$ at high values of $\gamma_{TAE}/\gamma_{Turb}$ for both simulation and experimental data. The transition from the increase to the reduction occurs at $\gamma_{TAE}/\gamma_{Turb} \simeq 0.5$. The energy and fraction of fast ions correspond to $T_{0f}/T_{0i} = 25$ and $n_{0f}/n_{0e} = 2.5\%$, respectively, in the GKNET simulations. These values are $T_{0f}/T_{0i} = 8$ and $n_{0f}/n_{0e} = 6.9\%$ for AUG39230, $T_{0f}/T_{0i} = 33.8$ and $n_{0f}/n_{0e} = 3\%$ for JET94701, $T_{0f}/T_{0i} = 11.9$ and $n_{0f}/n_{0e} = 5.9\%$ for DIII-D159243, and $T_{0f}/T_{0i} = 7$–$10$ and $n_{0f}/n_{0e} = 6$–$7\%$ for JET73224.

parameter that characterises the overall trend of changes in thermal heat transport due to the TAE–turbulence nonlinear interactions is the ratio $\gamma_{TAE}/\gamma_{Turb}$. Figure 2 shows the ratio of the ion heat flux in the presence of fast ions $Q_{iTAE+Turb}$ to that in the absence of the fast ions $Q_{iTurb}$ as a function of $\gamma_{TAE}/\gamma_{Turb}$. In our simulations, the TAE is unstable at $n = 2$ with growth rate $\gamma_{TAE}$, and the ITG mode or KBM is unstable in the high-wavenumber regime with the highest growth rate $\gamma_{Turb}$ at $n = 12$, which corresponds to $k_\theta \rho_i = 0.42$. The values of the growth rates $\gamma_{TAE}$ and $\gamma_{Turb}$ are shown in the "Methods" section. We have found that $Q_{iTAE+Turb}/Q_{iTurb}$ decreases with increasing $\gamma_{TAE}/\gamma_{Turb}$ for four scans: the fast-ion density gradient $L_{nf}$ scan of the turbulence at low normalised pressure $\beta$, the temperature gradient $L_T$ scan of the turbulence at low $\beta$, the $L_T$ scan of the turbulence at high $\beta$, and the $L_{nf}$ scan of the turbulence at high $\beta$. The heat flux is increased by the TAE–turbulence interactions, $Q_{iTAE+Turb}/Q_{iTurb} > 1$, at low values of $\gamma_{TAE}/\gamma_{Turb}$, whereas the heat flux is reduced, $Q_{iTAE+Turb}/Q_{iTurb} < 1$, at high values of $\gamma_{TAE}/\gamma_{Turb}$. The transition from the enhancement to the reduction occurs at $\gamma_{TAE}/\gamma_{Turb} \simeq 0.5$. It may be worth mentioning here that the normalised heat flux $Q_{iTAE+Turb}/Q_{iTurb}$ decreases as $\gamma_{TAE}/\gamma_{Turb}$ decreases at $\gamma_{TAE}/\gamma_{Turb} < 0.3$, as shown by the green and red curves, because the TAE becomes almost stable and its influence on the transport becomes weak.

## Comparison with experiments

To compare our simulation results with the experimental observations, we plot four points obtained from the analysis of ASDEX-Upgrade[12], JET[16,20,42], and DIII-D[22] in Fig. 2. The curve from our numerical simulations is in agreement with the points representing ASDEX-Upgrade discharge #39230 and JET discharge #94701, showing a reduction in thermal ion heat transport. The point representing the DIII-D discharge #159243 is consistent with an extrapolation of the curve from our simulation to a higher value of $\gamma_{TAE}/\gamma_{Turb}$. The point representing the JET discharge #73224 is in the stable regime $\gamma_{TAE}/\gamma_{Turb} < 0$, while it is plotted at $\gamma_{TAE}/\gamma_{Turb} = -0.1$ to save space. This point shows the suppression of the heat transport and is consistent with the curve from our simulation, because the normalised heat flux represented by the green and red curves approaches a small value as $\gamma_{TAE}/\gamma_{Turb}$ decreases in the regime $\gamma_{TAE}/\gamma_{Turb} < 0.3$. Hence, our parameter characterisation successfully reproduces the changes in thermal ion heat transport observed in the analysis of discharges in several machines. The characterisation is applicable to a variety of AEs such as TAE in JET#94701, reversed-shear AE (RSAE)[2] in DIII-D#159243, KBM/AE in AUG#39230, and beta-induced AE (BAE)[2] in JET#73224. We speculate that the same physics mechanism will apply to other AEs, as our theoretical prediction based on simulation results for the TAE agrees with the experimental observations for the RSAE in DIIID#159243 and BAE in JET#73224. In Fig. 2, the plotted experimental results spread over a range of fast ion energies and fast ion fractions, which are quantified by the ratio of fast ion to bulk ion temperature $T_{0f}/T_{0i}$ and the ratio between fast ion density and electron density $n_{0f}/n_{0e}$ in this study. These values are $T_{0f}/T_{0i} = 8$ and $n_{0f}/n_{0e} = 6.9\%$ for AUG#39230, $T_{0f}/T_{0i} = 33.8$ and $n_{0f}/n_{0e} = 3\%$ for JET#94701, $T_{0f}/T_{0i} = 11.9$ and $n_{0f}/n_{0e} = 5.9\%$ for DIII-D#159243, and $T_{0f}/T_{0i} = 7$–$10$ and $n_{0f}/n_{0e} = 6$–$7\%$ for JET#73224. We used $T_{0f}/T_{0i} = 25$ and $n_{0f}/n_{0e} = 2.5\%$ in the GKNET simulations. The points for JET#94701 and AUG#39230 exhibit similar reductions in heat transport, even though the values of these energies and fractions are significantly different. This is well captured by our characterisation in terms of $\gamma_{TAE}/\gamma_{Turb}$ and is in good agreement with our simulation results in Fig. 2. The reason behind this can be that the energy and fraction of fast ions affect the changes in turbulent transport and that of the growth rate of TAE in a similar way, as shown by GKNET simulations for different values of the energy and fraction of fast ions in "Methods". As a result, $\gamma_{TAE}/\gamma_{Turb}$ can characterise the trend of the experimental results for a wide range of various values of the energy and fraction of fast ions in Fig. 2. This characterisation is limited to a parameter regime in which the TAE–turbulence interactions are active. For extreme cases, such as when the fraction of fast ions is near 0% or 100%, we would not expect the TAE-turbulence interactions. The $\gamma_{TAE}/\gamma_{Turb}$ characterisation is also relevant when AEs influence turbulence via $E \times B$ flow-induced shearing. The enhancement of zonal flow amplitude by AEs is presented in refs. 14,16,17,20,21. is expected to be proportional to the amplitude of AE, which in turn correlates with $\gamma_{AE}$. This is very likely the reason why $\gamma_{TAE}/\gamma_{Turb}$ is a good parameter to characterise not only our simulation results but also other analyses of experimental data. An additional physical insight gained from our simulation studies is that the $E \times B$ flow-induced shearing of turbulence is mostly achieved by the large-scale TAE vortex flows represented by the coherent structure in Fig. 1b and c rather than axisymmetric zonal flows when $\gamma_{TAE}/\gamma_{Turb} > 0.7$, as shown below. See the "Methods" section for the evaluation of $Q_{iTAE+Turb}/Q_{iTurb}$ and $\gamma_{TAE}/\gamma_{Turb}$ from the experimental data.

The increase in the heat flux, $Q_{iTAE+Turb}/Q_{iTurb} > 1$, at small $\gamma_{TAE}/\gamma_{Turb}$ is not compared to the experimental data because we could not find any experiments in this very weak AE regime. The analysis in refs. 14,20. implies that the transport increases when the AE exceeds the marginal stability and becomes weakly unstable. The simulation results in refs. 14,20. may correspond to the enhancement of $Q_i$ in the $\gamma_{TAE}/\gamma_{Turb} < 0.3$ regime in our simulations. Further studies in this very weak AE regime are left for future work. On the other hand, the results in ref. 13 show an enhancement in the heat flux at $\gamma_{TAE}/\gamma_{Turb} = 1.62$. While this case is inconsistent with our parameter characterisation, the AE is significantly unstable in ref. 13 and can cause strong thermal ion heat flux. In other words, the interaction between the AE and turbulence does not play a dominant role in determining the thermal heat flux. This case is outside of the validity regime of our simple characterisation and suggests an upper limit of the suppression effect of AE on turbulent transport.

## Mechanism responsible for changes in heat transport

The changes in the heat flux $Q_i$ can be understood from redistribution of the wavenumber spectrum of $Q_i$. Figure 3a shows the toroidal wavenumber spectrum of the heat flux $Q_i(n)$ due to the ITG turbulence, where $Q_i = \sum_n Q_i(n)$. In the absence of TAE, the heat flux $Q_{iTurb}(n)$ peaks at $n = 12$. The

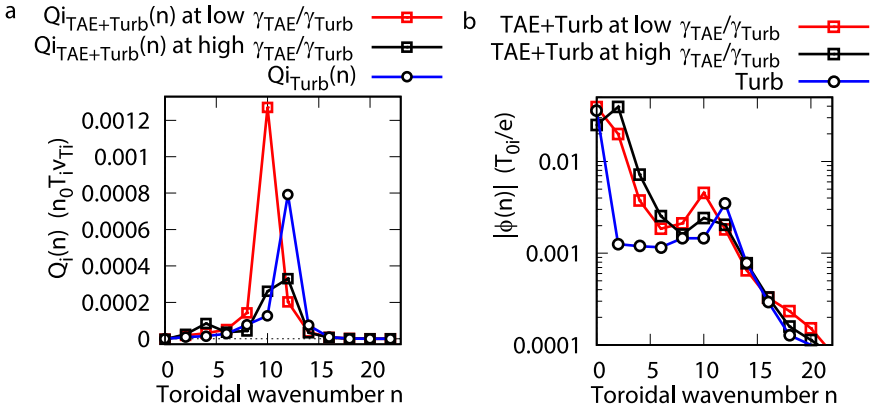



**Fig. 3 | Spectrum changes in ion heat transport in the presence of TAE. a** Toroidal wavenumber spectra of the thermal ion heat flux $Q_i(n)$ due to the turbulence at low $\beta$ with fast ions (TAE + Turb) and without fast ions (Turb), showing an increase in $Q_i$ at a low value of $\gamma_{TAE}/\gamma_{Turb}$ ($\gamma_{TAE}/\gamma_{Turb} = 0.48$, $R_0/L_{nf} = 28$) and a reduction in $Q_i$ at a high value of $\gamma_{TAE}/\gamma_{Turb}$ ($\gamma_{TAE}/\gamma_{Turb} = 0.66$, $R_0/L_{nf} = 33.5$), respectively, as computed by GKNET. Here, $n$ is the wavenumber for the toroidal coordinate $\zeta$ and $Q_i = \sum_n Q_i(n)$. **b** Toroidal wavenumber spectrum of perturbed electrostatic potential $\phi(n)$. The TAE–turbulence interactions shift the peak of the spectrum from high to low wavenumbers in (**a**) and (**b**). $Q_i(n)$ at $n = 10$ is the dominant contributor to the total $Q_i$. Consequently, the increase in $Q_i(n)$ at $n = 10$ causes the enhancement of $Q_i$ at low values of $\gamma_{TAE}/\gamma_{Turb}$, while the small $Q_i(n)$ at $n = 10$ causes the reduction in $Q_i$ at high values of $\gamma_{TAE}/\gamma_{Turb}$. The amplitude of the TAE represented by $|(n)|$ at $n = 2$ is larger than that of the zonal flow at $n = 0$ for TAE + Turb at a high value of $\gamma_{TAE}/\gamma_{Turb}$. This strong TAE reduces the thermal-ion heat flux $Q_i$ by shifting the peak of the spectrum from high to low wavenumbers.

TAE–turbulence interactions reduce the heat flux $Q_{iTAE+Turb}(n)$ from $Q_{iTurb}(n)$ at $n = 12$, while the interactions enhance the heat flux at $n = 10$ for both low and high values of $\gamma_{TAE}/\gamma_{Turb}$. The TAE–turbulence interactions also suppress the amplitude of electrostatic potential $|\phi(n)|$ at $n = 12$ and enhance $|\phi(n)|$ at $n = 10$ in Fig. 3b. These are similar to recent results by the GENE code showing that the AE–turbulence interactions shift the peak of the heat flux spectrum from high to low wavenumbers[43].

The spectrum of the electrostatic potential in Fig. 3b shows zonal flow production at $n = 0$ and excitation of TAE at $n = 2$. For the weaker drive of the TAE with $R_0/L_{nf} = 28$ (a low value of $\gamma_{TAE}/\gamma_{Turb}$), the amplitude of the TAE is smaller than that of zonal flows, and the energy transfer in the wavenumber space by the weak TAE is limited, as shown in Fig. 3a and b. The fluctuations cause strong heat transport at $n = 10$ because they are unstable against microinstability, resulting in the enhancement of $Q_i$ at low values of $\gamma_{TAE}/\gamma_{Turb}$, which is similar to the increase in $Q_i$ for the KBM turbulence at higher $\beta$[11]. Both the increase in the fluctuation amplitude and the modified phase difference between the electrostatic potential and temperature fluctuations contribute to the strong heat flux. For the stronger drive of TAE with $R_0/L_{nf} = 33.5$ (a high value of $\gamma_{TAE}/\gamma_{Turb}$), by contrast, the amplitude of the TAE is larger than that of zonal flows, and the TAE transfers the energy to a wide range of low $n$ values in Fig. 3b. The strongly excited fluctuations at low wavenumbers, such as $n = 4$, do not cause strong heat transport, as shown in Fig. 3a, leading to the reduction in $Q_i$. This is because the microinstability at $n = 4$ is stable, indicating that the electrostatic potential and temperature fluctuations are significantly out of phase, causing a small heat flux. Hence, the amplitude of the TAE influences the changes in ion heat transport through the redistribution of the heat flux spectrum.

## Large-scale flow shearing of turbulence

The mechanism of the reduction in turbulent transport is the large-scale E × B flow-induced shearing of microturbulence eddies, as quantified by the flow shearing shown in Fig. 1d. Figure 4 shows the TAE vortex flow shearing rate $\omega_{TAE} = \langle|d^2\phi_{TAE}/dr^2|\rangle$ and the zonal flow shearing rate $\omega_{E\times B} = \langle|d^2\phi_{ZF}/dr^2|\rangle$ as a function of $\gamma_{TAE}/\gamma_{Turb}$, where $\langle\cdots\rangle$ denotes the average over the radius. The zonal flow shearing rate is higher than the TAE vortex flow shearing rate at low values of $\gamma_{TAE}/\gamma_{Turb}$ and decreases with increasing $\gamma_{TAE}/\gamma_{Turb}$, while the TAE vortex flow shearing rate increases with $\gamma_{TAE}/\gamma_{Turb}$. The TAE vortex flow shearing rate becomes comparable with the zonal flow shearing rate at $\gamma_{TAE}/\gamma_{Turb} \simeq 0.7$ for the turbulence at low $\beta$, and is higher than the zonal flow shearing rate at $\gamma_{TAE}/\gamma_{Turb} > 0.4$ for the turbulence at high $\beta$. Thus, the heat flux $Q_{iTAE+Turb}$ is regulated by the large-scale E × B flow, i.e., the zonal flow and TAE vortex flow, while the difference between $Q_{iTAE+Turb}$ and $Q_{iTurb}$ is mainly caused by the TAE vortex flow at large $\gamma_{TAE}/\gamma_{Turb}$. This correlation of changes in the TAE vortex flow shearing rate and changes in turbulent transport is similar to the well-known reduction of microturbulence eddies' radial size due to axisymmetric E × B flow shear[44] where a significant reduction in turbulent transport has been observed when the E × B shearing rate, $\omega_{E\times B}$ in tokamak geometry[37], exceeds $\gamma_{Turb}$. The E × B flow shearing rate $\omega_{E\times B}$ at high $\beta$ is larger than that at low $\beta$. This is because the linear growth rate of the KBM at high $\beta$ is significantly higher than that of the ITG mode at low $\beta$, as shown in Fig.5, so that the amplitude of the fluctuations of the KBM that drives the zonal flows is much larger than that of the ITG mode. As a result, $\omega_{E\times B}$ at high $\beta$ is larger than that at low $\beta$. It is noteworthy that the zonal flow-induced turbulence shearing and the AE vortex flow-induced shearing of turbulence eddies share a common physical

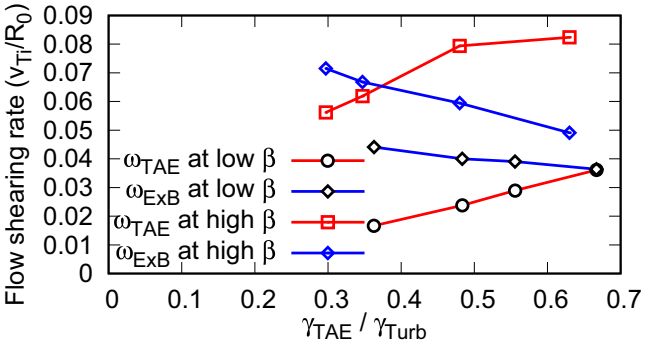



**Fig. 4 | Large-scale flow shearing of turbulence eddies.** TAE vortex flow shearing rate $\omega_{TAE} = \langle|d^2\phi_{TAE}/dr^2|\rangle$ and zonal E×B flow shearing rate $\omega_{E\times B} = \langle|d^2\phi_{ZF}/dr^2|\rangle$ as a function of $\gamma_{TAE}/\gamma_{Turb}$ for the fast-ion density gradient ($L_{nf}$) scan of the turbulence at low $\beta$ and the temperature gradient ($L_T$) scan of the turbulence at high $\beta$ as simulated by GKNET, where $\langle\cdots\rangle$ denotes the average over the radius $r$. The TAE vortex flow shearing rate becomes comparable to the zonal flow shearing rate at $\gamma_{TAE}/\gamma_{Turb} \simeq 0.7$ at low $\beta$, and becomes higher than the zonal flow shearing rate at $\gamma_{TAE}/\gamma_{Turb} > 0.4$ at high $\beta$.

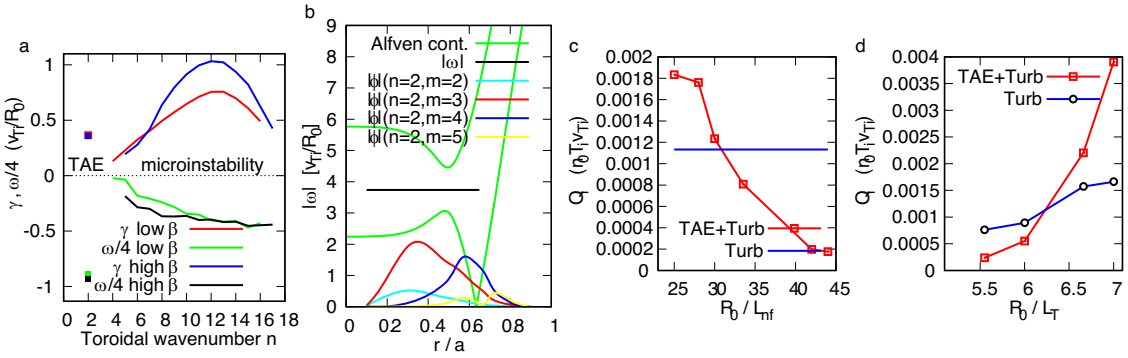



**Fig. 5 | Linear dispersion relation of toroidal Alfvénic eigenmode (TAE) and microinstabilities, and thermal ion heat flux. a** Linear growth rate $\gamma$ and real frequency $\omega$ of TAE and microinstabilities simulated by GKNET for two values of $\beta$ as a function of the toroidal wavenumber $n$. The microinstability is the ion-temperature gradient (ITG) mode at low $\beta$ ($\beta = 0.64\%$) for $R_0/L_T = 6.66$ and $R_0/L_{nf} = 28$, as shown in **c** and is the kinetic ballooning mode (KBM) at high $\beta$ ($\beta = 1.28\%$) for $R_0/L_T = 6.66$ and $R_0/L_{nf} = 33.5$, as shown in **d**, where $R_0/L_T$ and $R_0/L_{nf}$ are the logarithmic gradients normalised by the major radius of the torus $R_0$. The TAE is unstable at a low wavenumber ($n = 2$), whereas the microinstabilities are unstable at high wavenumbers ($n \geq 6$). **b** Alfvén wave continuum of $n = 2$ mode, real frequency of $n = 2$ TAE at high $\beta$ in **a**, and eigenfunction $|\phi(n,m)|$. **c** Thermal ion heat flux $Q_i$ in the presence of TAE driven by fast ions (TAE + Turb) and that in the absence of fast ions (Turb) as a function of the fast-ion density gradient $R_0/L_{nf}$ for turbulence at low $\beta$ (ITG) as simulated by GKNET. The heat flux $Q_i$ due to the TAE-turbulence interaction (TAE + Turb) decreases with increasing drive of TAE $R_0/L_{nf}$, and the thermal ion heat transport is suppressed in the presence of a stronger TAE. **d** Heat flux as a function of the bulk temperature gradient $R_0/L_T$ for turbulence at high $\beta$ (KBM). In the presence of TAE (TAE + Turb), the TAE–turbulence interaction increases $Q_i$ at high gradients, whereas the interaction decreases $Q_i$ at low gradients.

mechanism. The former has been well-established by previous works. In addition, our work demonstrates that the latter can be a main mechanism for a relatively large value of $\gamma_{TAE}/\gamma_{Turb}$. The TAE vortex flow shearing can be an extension of the shearing by axisymmetric zonal flows, and thus the influence of the TAE vortex flow shearing can be related to the parameter $\gamma_{TAE}/\gamma_{Turb}$. We remark that zonal flow-induced shearing can be enhanced and dominate the vortex flow-induced shearing with increasing $\gamma_{TAE}$ when there are multiple unstable TAEs[45]. However, the physics of vortex-induced shearing and that of zonal flow-induced shearing are very similar, and characterisation by the parameter is still useful even in that case.

The TAE vortex flow is different from the zonal flow by having a non-zero real frequency and a spatial variation in the poloidal direction. If the TAE vortex flow pattern changes in time too rapidly, it can reduce the effectiveness of shearing microturbulence eddies[46]. However, the TAE rotation rate slows down significantly in the nonlinear saturation regime. Therefore, the TAE vortex induced shearing is effective and exhibits a similar suppression effect on the turbulence eddy size as familiar from the vortex flow in magnetic islands[47–50]. In addition, concerning the mode structure of TAE in the poloidal direction, its effect on the shearing is weak compared to $(d^2\phi/dr^2)$[38,51].

## Discussion

We have investigated the influence of fast-ion-driven AEs on the plasma thermal confinement, which is a critical fusion-relevant issue. We have identified a key parameter that characterises the changes in the heat transport of thermal ions due to nonlinear interactions between the TAE driven by fast ions and the microturbulence driven by the ion-temperature gradient in tokamak plasmas. The parameter is the ratio of the growth rate of the TAE to that of the microturbulence, $\gamma_{TAE}/\gamma_{Turb}$, and the thermal heat transport is mitigated at $\gamma_{TAE}/\gamma_{Turb} > 0.5$. This characterisation based on the key dimensionless parameter, successfully covers the trend of experimental results from JET, ASDEX-Upgrade, and DIII-D, where a variety of AEs play a role. The experimental results indicate lower values of normalised heat fluxes compared with those from GKNET. This observation may imply that the suppression effect of AEs on turbulent transport is more pronounced than what is anticipated by the GKNET simulations. While we cannot justify that the growth rate describes the nonlinear saturated state in general a priori, it turns out to be a useful indicator to characterise the changes in turbulent transport due to the presence of TAE for the cases we have simulated. Of course, there exists a theoretical possibility of one type of instability with a lower growth rate but with a larger scale may dominate turbulent transport in the nonlinear saturated regime[52,53]. Although it is parameterised by the linear growth rates, the underlying physical mechanism for the transport reduction at high values of $\gamma_{TAE}/\gamma_{Turb}$ is the shearing of microturbulence eddies by the large-scale $E \times B$ flow associated with TAE. It is noted that the simple parameter $\gamma_{TAE}/\gamma_{Turb}$ can be calculated from linear simulations, which require significantly less computational resources than nonlinear simulations. Because of this reduced numerical cost, the parameter can be useful not only in understanding the results from current experiments, but also as the first step in predicting the performance of burning plasmas in future devices. We note that multiple fast-ion species effects are not included because of numerical reasons. Simulations with multiple fast-ion species and a much higher energy of fast ions, such as 3.5 MeV alpha particles, will be pursued in the near future, as well as the validation of the parameter characterisation for experimental magnetic field configuration, density, and temperature profiles.

## Methods

### Simulation details

Turbulent transport in the presence of the TAE–turbulence interaction is simulated using the global gyrokinetic simulation code GKNET[39]. The time evolution of the distribution function is solved based on the gyrokinetic equation[40,41] coupled with Maxwell's equation to obtain the electrostatic and vector potentials. The gyrokinetic equation is derived from the Boltzmann equation by removing the gyrophase angle dependence of the particle distribution function coming from fast cyclotron motion around the ambient magnetic field $\boldsymbol{B}_0$[40,41], and describes the spatiotemporal evolution of the distribution function $f(r, \theta, \zeta, v_{\|}, \mu, t)$, where the two velocity coordinates are the parallel velocity $v_{\|}$ and magnetic moment $\mu = m\,|\,\boldsymbol{v}_{\perp}|^2/(2B_0)$, where $\boldsymbol{v} = v_{\|}\boldsymbol{B}_0/B_0 + \boldsymbol{v}_{\perp}$. The toroidal coordinates of the particle gyrocenter position $(r, \theta, \zeta)$ are shown in Fig. 1a. The Fourier expansion is used along the toroidal direction, so that the distribution function can be written as $f(r, \theta, \zeta, v_{\|}, \mu, t) = \sum_n f_n(r, \theta, v_{\|}, \mu, t)\exp(in\zeta)$, where $n$ is the toroidal wavenumber. The nonlinear interactions between the TAE, turbulence, and zonal flows are represented in terms of the Poisson bracket in the gyrokinetic equation. The nonlinear interplay between different modes is validated by confirming the conservation of perturbed entropy in the toroidal wavenumber space in GKNET[54].

To understand the basic physics of the interactions between TAE and turbulence, we consider typical turbulence driven by the ion-temperature gradient (ITG) and typical TAE in a normal magnetic shear tokamak plasma with a circular cross-section instead of an experimental configuration. Global simulations are necessary to capture the global spatial structure of TAE, which has a low toroidal wavenumber. We consider a typical case in which the TAE directly interacts with the ITG turbulence with the gap of the Alfvén wave continuum located at the middle of the minor radius $r$. Here, we describe the setup of the nonlinear simulations of this plasma. The background magnetic field $\boldsymbol{B}_0 = (0, B_{\theta 0}, B_{\zeta 0})$ is characterised by the safety factor $q(r) = rB_{\zeta 0}/(R_0 B_{\theta 0})$, representing the twist of the magnetic field lines, where $R_0$ is the major radius of the torus. The safety factor, the temperature and density profiles are $q(r) = 1.65 + 1.5(r/a + 0.15)^6$, $n_s(r) = n_{0s}\exp[-\delta_r/L_{ns}\tanh((r-r_0)/\delta_r)]$ and $T_s(r) = T_{0s}\exp[-\delta_r/L_T\tanh((r-r_0)/\delta_r)]$, respectively, where $r_0 = a/2$, $\delta_r = 0.3a$ and $R_0/L_{ni} = 2.22$. Here, $s$ = e, i, and f represent the electron, ion, and fast-ion species, respectively, and $a$ is the minor radius and $a/R_0 = 0.2$. There is no source or sink of heat and particles in the system. The simulation domain is $0.1 \le r/a \le 0.9$, and fluctuations are set to vanish at the boundary. Plasma parameters are $\rho* = 1/100$, $T_{0f}/T_{0i} = 25$, $m_i/m_e = 100$, $n_{0i}/n_{0e} = 0.975$ and $n_{0f}/n_{0e} = 0.025$, and $N_r \times N_\theta \times N_{v\parallel} \times N_\mu = 128 \times 256 \times 64 \times 16$ grid points are employed[11,39]. The toroidal direction is treated with spectral methods with 30 even modes, and the collisions are calculated using the Lenard–Bernstein operator. The simulation cost for studying the interaction between the TAE and turbulence is very high because of the following requirements that should be satisfied simultaneously. The first is the time-scale resolution and duration of the simulation. The highest frequency of fluctuations in the gyrokinetic simulations of plasmas with fast ions is the real frequency of the TAE, denoted as $\omega_A$, and $\omega_A \delta t = 0.02 \ll 1$ is satisfied in our simulations, where $\delta t$ is the minimum time-step width. We successfully obtained the nonlinear saturated state of TAE and turbulence in the presence of their nonlinear interactions. If the conditions were not satisfied, a nonlinear saturated state could not be established. This observation also demonstrates that the simulation duration was sufficiently long. Second, simulating turbulence requires high resolution in the configuration space, particularly in the directions normal to the magnetic field, to resolve the fine-scale structure of turbulence eddies. In addition, simulating the TAE requires a high resolution in the velocity space to capture the wave-particle resonance, especially in the parallel direction along the field line.

### Growth rate and frequency of TAE and microturbulence

When the amplitude of the fluctuation is infinitesimally small, the nonlinear terms in the gyrokinetic equation can be neglected. As a result, the time evolution of the Fourier components of the fluctuations can be written in the form of $f_n = g_n \exp(\gamma(n)t - i\omega(n)t)$, where $\gamma(n)$ and $\omega(n)$ are the linear growth rate and real frequency of the fluctuation for a toroidal wavenumber $n$, respectively. Figure 5a shows the linear growth rate and real frequency as functions of toroidal wavenumber. The TAE is unstable at a low toroidal wavenumber $n = 2$, and thus $\gamma_{TAE} = \gamma(n = 2)$. The microinstabilities are unstable at high wavenumbers $n \ge 6$, and their growth rates peak at $n = 12$; therefore $\gamma_{Turb} = \gamma(n = 12)$. The microinstability is the ITG mode for low $\beta$ ($\beta = 0.64\%$), while it is the kinetic ballooning mode (KBM) for high $\beta$ ($\beta = 1.28\%$). The real frequency of the TAE $\omega = 0.3\ [v_A/R_0] = 3.7\ [v_{Ti}/R_0]$ for high $\beta$ lies within the gap in the Alfvén wave continuum, as shown in Fig. 5b. We will report the benchmarking of GKNET for some experimental cases in our next paper.

### Definition of ion heat flux

The turbulent heat flux of thermal ions is given by

$$Q_i = \mathrm{Re}\left[\left\langle -\frac{1}{r}\frac{\partial\langle\phi\rangle_i}{\partial\theta}\frac{p_i}{B}\right\rangle + \left\langle\frac{1}{r}\frac{\partial\langle A_\parallel\rangle_i}{\partial\theta}\frac{q_i}{B}\right\rangle\right] \quad (1)$$

where $p_i = \int\langle(m_i v_\parallel^2/2 + \mu B_0)f_i\rangle_i\,dv^3$ and $q_i = \int\langle v_\parallel(m_i v_\parallel^2/2 + \mu B_0)f_i\rangle_i\,dv^3$, where $\langle\ldots\rangle_i$ and $\langle\ldots\rangle$ denote the gyro-average and flux surface average, respectively. The ion distribution function $f_i$, electrostatic potential $\phi$, and vector potential $A_\parallel$ are obtained from nonlinear gyrokinetic simulations using the GKNET code. In the figures, $Q_i$ is averaged over the radius $r$ and over a time window in the nonlinear steady state of turbulence.

### Plasma profile scans of thermal ion heat flux

Thermal temperature gradient $R_0/L_T$ and fast ion density gradient $R_0/L_{nf}$ scans of the thermal ion heat flux $Q_i$ were performed using the GKNET code. The logarithmic gradient is normalised by the major radius of the torus $R_0$. The heat flux $Q_i$ in the presence of fast ions is indicated by "TAE + Turb", while $Q_i$ in the absence of fast ions is indicated by "Turb". Figure 5c shows that $Q_i$ due to the turbulence at low $\beta$ with fast ions (TAE + Turb) decreases with increasing drive of TAE $R_0/L_{nf}$, while $Q_i$ without fast ions (Turb) remains unchanged. Thus, the thermal ion heat transport is suppressed in the presence of a stronger TAE. It is useful to note that the influence of nonlinear interactions between the TAE and turbulence on the thermal heat transport correlates with the linear growth rate of the TAE, $\gamma_{TAE}$. Figure 5d shows that the thermal ion heat flux $Q_i$ due to turbulence at high $\beta$ (Turb) increases with increasing temperature gradient $R_0/L_T$, as expected. In the presence of TAE driven by fast ions (TAE + Turb), the TAE–turbulence interaction increases $Q_i$ at high gradients, whereas the interaction decreases $Q_i$ at low gradients. Therefore, there also exists a correlation between the influence of TAE–turbulence nonlinear interactions on thermal transport and the linear growth rate of the microinstability $\gamma_{Turb}$, which is a strong function of $R_0/L_T$. The same behaviour with respect to $R_0/L_T$ is found for turbulence at low $\beta$. Thus, these results are common to both turbulence at low $\beta$ (ITG) and turbulence at high $\beta$ (KBM). We verified that the changes in the heat flux are not due to profile relaxation caused by the growth of the TAE.

Here, we briefly discuss the influence of the energy and fraction of fast ions on changes in turbulent transport. Figure 6 shows that the values of the energy and fraction of fast ions affect the changes in turbulent transport and the growth rate of the TAE in a similar way. Thus, $\gamma_{TAE}/\gamma_{Turb}$ can characterise the trend of the changes in turbulent transport when the interaction between the TAE and turbulence is active.

### Evaluation of heat flux and key parameter from experimental data

The values of the normalised heat flux $Q_{iTAE+Turb}/Q_{iTurb}$ and the key parameter $\gamma_{TAE}/\gamma_{Turb}$ are approximately evaluated by using data from the published work for ASDEX-Upgrade discharge #39230[12], DIII-D discharge #159243[22], JET discharge #94701[16,42], and JET discharge #73224[20]. For example, for ASDEX-U#39230[12], $\gamma_{AE} = 0.095\ [c_s/a]$ and $\gamma_{Turb} = 0.18\ [c_s/a]$, so that $\gamma_{AE}/\gamma_{Turb} = 0.53$. The normalised heat flux is approximated to $Q_{iTAE+Turb}/Q_{iTurb} \simeq 0.3$ for the average over $0.3 \le \rho_{tor} \le 0.6$. For DIII-D#159243[22], $\gamma_{AE} = 3.23 \times 10^4$ [1/s] and $\gamma_{Turb} = 2.2 \times 10^4$ [1/s] as written in page 3, so that

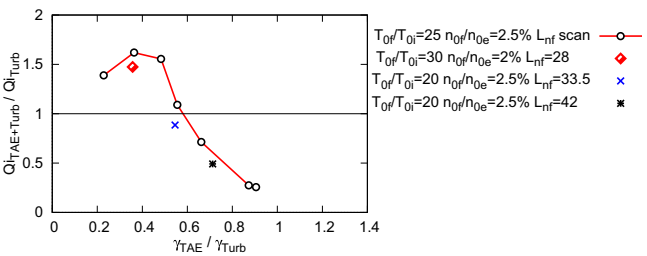



**Fig. 6 | Influence of the energy and fraction of fast ions on changes in turbulent transport.** Normalised thermal ion heat flux with fast ions $Q_{iTAE+Turb}/Q_{iTurb}$ as a function of $\gamma_{TAE}/\gamma_{Turb}$. The points connected by a red curve correspond to the fast-ion density gradient $L_{nf}$ scan of the GKNET simulations for ITG turbulence at low $\beta$ for the energy and fraction of fast ions $T_{0f}/T_{0i} = 25$ and $n_{0f}/n_{0e} = 2.5\%$, respectively. The other three points represent $Q_{iTAE+Turb}/Q_{iTurb}$ for the three sets of values of different energies and fractions of fast ions: $T_{0f}/T_{0i} = 30$, $n_{0f}/n_{0e} = 2\%$ and $L_{nf} = 28$; $T_{0f}/T_{0i} = 20$, $n_{0f}/n_{0e} = 2.5\%$ and $L_{nf} = 33.5$; $T_{0f}/T_{0i} = 20$, $n_{0f}/n_{0e} = 2.5\%$ and $L_{nf} = 42$.

$\gamma_{AE}/\gamma_{Turb} = 1.47$. The normalised heat flux is approximated to $Q_{iTAE+Turb}/Q_{iTurb} \simeq 0.4$ based on the statement "a reduction of the thermal ion heat transport by more than a factor of 2" in the "Abstract" section[22].

## Data availability

The data that support the findings of this study are available on request from the corresponding author.

## Code availability

The GKNET code is available from the corresponding author upon reasonable request.

Received: 23 May 2025; Accepted: 24 October 2025;
Published online: 28 November 2025

## References

1. Horton, W. Drift waves and transport. *Rev. Mod. Phys.* **71**, 735–778 (1999).
2. Chen, L. & Zonca, F. Physics of Alfvén waves and energetic particles in burning plasmas. *Rev. Mod. Phys.* **88**, 015008 (2016).
3. Cheng, C. Z., Chen, L. iu & Chance, M. S. High-n ideal and resistive shear Alfvén waves in tokamaks. *Ann. Phys.* **161**, 21–47 (1985).
4. Cheng, C. Z. & Chance, M. S. Low-n shear Alfvén spectra. *Phys. Fluids* **29**, 3695–3701 (1986).
5. Heidbrink, W. W., Strait, E. J., Doyle, E., Sager, G. & Snider, R. T. An investigation of beam driven Alfvén instabilities in the DIII-D tokamak. *Nucl. Fusion* **31**, 1635 (1991).
6. Spong, D. A., Carreras, B. A. & Hedrick, C. L. Nonlinear evolution of the toroidal Alfvén instability using a gyrofluid model. *Phys. Plasmas* **1**, 1503–1510 (1994).
7. Todo, Y. & Sato, T. Linear and nonlinear particle-magnetohydrodynamic simulations of the toroidal Alfvén eigenmode. *Phys. Plasmas* **5**, 1321–1327 (1998).
8. Bierwage, A. et al. Simulations tackle abrupt massive migrations of energetic beam ions in a tokamak plasma. *Nat. Commun.* **9**, 3282 (2018).
9. Pinches, S. D. et al. Energetic ions in ITER plasmas. *Phys. Plasmas* **22**, 021807 (2015).
10. Fasoli, A. et al. Chapter 5: Physics of energetic ions. *Nucl. Fusion* **47**, S264 (2007).
11. Ishizawa, A., Imadera, K., Nakamura, Y. & Kishimoto, Y. Multi-scale interactions between turbulence and magnetohydrodynamic instability driven by energetic particles. *Nucl. Fusion* **61**, 114002 (2021).
12. Di Siena, A. et al. Impact of supra-thermal particles on plasma performance at ASDEX Upgrade with GENE-Tango simulations. *Nucl. Fusion* **64**, 066020 (2024).
13. Biancalani, A. et al. Gyrokinetic investigation of Alfvén instabilities in the presence of turbulence. *Plasma Phys. Control. Fusion* **63**, 065009 (2021).
14. Di Siena, A. et al. Electromagnetic turbulence suppression by energetic particle driven modes. *Nucl. Fusion* **59**, 124001 (2019).
15. Mazzi, S. et al. Enhanced performance in fusion plasmas through turbulence suppression by megaelectronvolt ions. *Nat. Phys.* **18**, 776–782 (2022).
16. Mazzi, S. et al. Gyrokinetic study of transport suppression in JET plasmas with MeV-ions and toroidal Alfvén eigenmodes. *Plasma Phys. Control. Fusion* **64**, 114001 (2022).
17. Garcia, J. & JET Contributors. Electromagnetic and fast ions effects as a key mechanism for turbulent transport suppression at JET. *Plasma Phys. Control. Fusion* **64**, 104002 (2022).
18. Han, H. et al. A sustained high-temperature fusion plasma regime facilitated by fast ions. *Nature* **609**, 269–275 (2022).
19. Liu, P. et al. Regulation of Alfvén eigenmodes by microturbulence in fusion plasmas. *Phys. Rev. Lett.* **128**, 185001 (2022).
20. Di Siena, A. et al. How accurate are flux-tube (local) gyrokinetic codes in modeling energetic particle effects on core turbulence?. *Nucl. Fusion* **63**, 106012 (2023).
21. Garcia, J. et al. Stable Deuterium-Tritium plasmas with improved confinement in the presence of energetic-ion instabilities. *Nat. Commun.* **15**, 7846 (2024).
22. Liu, P. et al. Cross-scale interaction between microturbulence and meso-scale reversed shear Alfvén eigenmodes in DIII-D plasmas. *Nucl. Fusion* **64**, 076007 (2024).
23. Citrin, J. & Mantica, P. Overview of tokamak turbulence stabilization by fast ions. *Plasma Phys. Control. Fusion* **65**, 033001 (2023).
24. Na, Y. S. et al. How fast ions mitigate turbulence and enhance confinement in tokamak fusion plasmas. *Nat. Rev. Phys.* **7**, 190–202 (2025).
25. Di Siena, A., G¨orler, T., Doerk, H., Poli, E. & Bilato, R. Fast-ion stabilization of tokamak plasma turbulence. *Nucl. Fusion* **58**, 054002 (2018).
26. Bonanomi, N. et al. Turbulent transport stabilization by ICRH minority fast ions in low rotating JET ILW L-mode plasmas. *Nucl. Fusion* **58**, 056025 (2018).
27. Di Siena, A. et al. New high-confinement regime with fast ions in the core of fusion plasmas. *Phys. Rev. Lett.* **127**, 025002 (2021).
28. Hahm, T. S., Choi, G. J., Park, S. J. & Na, Y.-S. Fast ion effects on zonal flow generation: A simple model. *Phys. Plasmas* **30**, 072501 (2023).
29. Cho, Y. W. & Hahm, T. S. Residual zonal flows in tokamaks in the presence of energetic ions. *Nucl. Fusion* **59**, 066026 (2019).
30. Choi, G. J., Diamond, P. H. & Hahm, T. S. On how fast ions enhance the regulation of drift wave turbulence by zonal flows. *Nucl. Fusion* **64**, 016029 (2024).
31. Mishchenko, A. et al. Gyrokinetic particle-in-cell simulations of electromagnetic turbulence in the presence of fast particles and global modes. *Plasma Phys. Control. Fusion* **64**, 104009 (2022).
32. Brochard, G. et al. Saturation of fishbone instability by self-generated zonal flows in tokamak plasmas. *Phys. Rev. Lett.* **132**, 175101 (2024).
33. Howes, G. G. et al. Gyrokinetic Simulations of Solar Wind Turbulence from Ion to Electron Scales. *Phys. Rev. Lett.* **107**, 035004 (2011).
34. Chen, C.-C. & Diamond, P. H. Potential vorticity mixing in a tangled magnetic field. *Astrophys. J.* **892**, 24 (2020).
35. Pueschel, M. J., Jenko, F., Told, D. & Buchner, J. Gyrokinetic simulations of magnetic reconnection. *Phys. Plasmas* **18**, 112102 (2011).
36. Diamond, P. H. et al. Dynamics of transition to enhanced confinement in reversed magnetic shear discharges. *Phys. Rev. Lett.* **78**, 1472 (1997).
37. Hahm, T. S. & Burrell, K. H. Flow shear induced fluctuation suppression in finite aspect ratio shaped tokamak plasma. *Phys. Plasmas* **2**, 1648–1651 (1995).
38. Diamond, P. H., Itoh, S. I., Itoh, K. & Hahm, T. S. Zonal flows in plasmas —a review. *Plasma Phys. Control. Fusion* **47**, R35 (2005).
39. Ishizawa, A., Imadera, K., Nakamura, Y. & Kishimoto, Y. Global gyrokinetic simulation of turbulence driven by kinetic ballooning mode. *Phys. Plasmas* **26**, 082301 (2019).
40. Hahm, T. S., Lee, W. W. & Brizard, A. Nonlinear gyrokinetic theory for finite-beta plasmas. *Phys. Fluids* **31**, 1940–1948 (1988).
41. Brizard, A. J. & Hahm, T. S. Foundations of nonlinear gyrokinetic theory. *Rev. Mod. Phys.* **79**, 421–468 (2007).
42. Di Siena, A., Merlo, G., Navarro, A. B., Gorler, T. & Jenko, F. Reassessing the impact of megaelectronvolt ions in fusion plasmas via gyrokinetic simulations. Preprint at https://doi.org/10.48550/arXiv.2306.10780 (2023).
43. Di Siena, A. et al. Understanding turbulence suppression in JET D-T plasma with highly energetic fast ions via global gyrokinetic GENE simulations. *Nucl. Fusion* **65**, 086019 (2025).
44. Biglari, H., Diamond, P. H. & Terry, P. W. Influence of sheared poloidal rotation on edge turbulence. *Phys. Fluids B* **2**, 1–4 (1990).

45. Spong, D. A. et al. Nonlinear dynamics and transport driven by energetic particle instabilities using a gyro-Landau closure model. *Nucl. Fusion* **61**, 116061 (2021).
46. Hahm, T. S. et al. Shearing rate of time-dependent ExB flow. *Phys. Plasmas* **6**, 922–926 (1999).
47. Hahm, T. S., Kim, Y. J., Diamond, P. H. & Choi, G. J. Anisotropic E x B shearing rate in a magnetic island. *Phys. Plasmas* **28**, 022302 (2021).
48. Choi, G. J. & Hahm, T. S. Long term vortex flow evolution around a magnetic island in tokamaks. *Phys. Rev. Lett.* **128**, 225001 (2022).
49. Poli, E. et al. Gyrokinetic and gyrofluid investigation of magnetic islands in tokamaks. *Plasma Phys. Control. Fusion* **52**, 124021 (2010).
50. Ishizawa, A., Kishimoto, Y. & Nakamura, Y. Multi-scale interactions between turbulence and magnetic islands and parity mixture—a review. *Plasma Phys. Control. Fusion* **61**, 054006 (2019).
51. Hahm, T. S. & Burrell, K. H. Role of flow shear in enhanced core confinement regimes. *Plasma Phys. Control. Fusion* **38**, 1427 (1996).
52. Matsukiyo, S. & Scholer, M. On microinstabilities in the foot of high Mach number perpendicular shocks. *J. Geophys. Res.* **111**, A06104 (2006).
53. Villafana, W. et al. 2D radial-azimuthal particle-in-cell benchmark for E × B discharges. *Plasma Sources Sci. Technol.* **30**, 075002 (2021).
54. Masui, H. et al. Global saturation physics of ion temperature gradient turbulence in finite normalized pressure tokamaks. *Nucl. Fusion* **62**, 074001 (2022).

## Acknowledgements

This work was supported by the Japanese Ministry of Education, Culture, Sports, Science and Technology (Grant No. 24K06991), and by the National Research Foundation of Korea (NRF) funded by the Korean government (Ministry of Science and ICT) (Grant No. 2023R1A2C100773512). A part of this work has been carried out during TSH's visits to Kyoto University under the project, Centre for Transport Barrier Formation in the Plasma Science Centre for the Promotion of Interdisciplinary Education and Research. E.P. would like to thank the Graduate School of Energy Science of Kyoto University for its hospitality and support during the early phase of this work, and Thomas Hayward-Schneider, Philipp Lauber, and Xin Wang for useful discussions.

## Author contributions

A.I. proposed and performed numerical simulations and analysed the data. E.P., A.D.S., and T.S.H. contributed to the physical interpretation. All authors contributed to the preparation of the manuscript.

## Competing interests

The authors declare no competing interests.

## Additional information

**Correspondence** and requests for materials should be addressed to Akihiro Ishizawa.

**Peer review information** *Communications Physics* thanks the anonymous reviewers for their contribution to the peer review of this work.

**Reprints and permissions information** is available at http://www.nature.com/reprints

**Publisher's note** Springer Nature remains neutral with regard to jurisdictional claims in published maps and institutional affiliations.

**Open Access** This article is licensed under a Creative Commons Attribution 4.0 International License, which permits use, sharing, adaptation, distribution and reproduction in any medium or format, as long as you give appropriate credit to the original author(s) and the source, provide a link to the Creative Commons licence, and indicate if changes were made. The images or other third party material in this article are included in the article's Creative Commons licence, unless indicated otherwise in a credit line to the material. If material is not included in the article's Creative Commons licence and your intended use is not permitted by statutory regulation or exceeds the permitted use, you will need to obtain permission directly from the copyright holder. To view a copy of this licence, visit http://creativecommons.org/licenses/by/4.0/.

© The Author(s) 2025